PASJ: Publ. Astron. Soc. Japan **60**, 1039–1050, 2008 October 25

Variable Asymmetry of the Circumstellar Envelope in IK Tauri Traced by SiO Maser Emission

Naoko MATSUMOTO,[1,6] Toshihiro OMODAKA,[1,2] Hiroshi IMAI,[1,2] Rie SHIMIZU,[1] Takeshi BUSHIMATA,[3,4] Yoon Kyung CHOI,[5] Tomoya HIROTA,[3,6] Mareki HONMA,[3,6] Noritomo INOMATA,[1] Kenzaburo IWADATE,[7] Takaaki JIKE,[7] Seiji KAMENO,[1,2] Osamu KAMEYA,[6,7] Ryuichi KAMOHARA,[3] Yukitoshi KAN-YA,[8] Noriyuki KAWAGUCHI,[3,6] Hideyuki KOBAYASHI,[3,4,5,6,7] Seisuke KUJI,[7] Tomoharu KURAYAMA,[3] Toshihisa MAEDA,[1] Seiji MANABE,[6,7] Takeshi MIYAJI,[3,4] Akiharu NAKAGAWA,[2] Takumi NAGAYAMA,[1] Koichiro NAKASHIMA,[1] Chung Sik OH,[3,5] Tomoaki OYAMA,[3] Satoshi SAKAI,[7] Seiichiro SAKAKIBARA,[1] Tetsuo SASAO,[9,10] Katsuhisa SATO,[7] Katsunori M. SHIBATA,[3,4,6] Motonobu SHINTANI,[1] Yoshiaki SOFUE,[1,2] Kasumi SORA,[1] Hiroshi SUDA,[7] Yoshiaki TAMURA,[6,7] Miyuki TSUSHIMA,[1] and Kazuyoshi YAMASHITA[6]

[1]*Graduate School of Science and Engineering, Kagoshima University, 1-21-35 Korimoto, Kagoshima, Kagoshima 890-0065*
[2]*Faculty of Science, Kagoshima University, 1-21-35 Korimoto, Kagoshima, Kagoshima 890-0065*
[3]*Mizusawa VERA Observatory, National Astronomical Observatory of Japan, 2-21-1 Osawa, Mitaka, Tokyo 181-8588*
[4]*Space VLBI Project, National Astronomical Observatory of Japan, 2-21-1 Osawa, Mitaka, Tokyo 181-8588*
[5]*Department of Astronomy, Graduate School of Science, The University of Tokyo, 7-3-1 Hongo, Bunkyo-ku, Tokyo 113-0033*
[6]*Department of Astronomical Sciences, Graduate University for Advanced Studies, 2-21-1 Osawa, Mitaka, Tokyo 181-8588*
[7]*Mizusawa VERA Observatory, National Astronomical Observatory of Japan, 2-12 Hoshi-ga-oka, Mizusawa-ku, Oshu-shi, Iwate 023-0861*
[8]*Department of Astronomy, Yonsei University, 134 Shinchong-dong, Seodaemun-gu, Seoul 120-749, Republic of Korea*
[9]*Department of Space Survey and Information Technology, Ajou University, Suwon 443-749, Republic of Korea*
[10]*Korean VLBI Network, Korea Astronomy and Space Science Institute, P.O.Box 88, Yonsei University, 134 Shinchon-dong, Seodaemun-gu, Seoul 120-749, Republic of Korea*
matsumoto@astro.sci.kagoshima-u.ac.jp

(Received 2008 February 29; accepted 2008 August 17)

Abstract

We observed the SiO ($v = 1$ and $v = 2$, $J = 1$–0) maser emissions toward the Mira variable IK Tauri (IK Tau, NML Tau, IRC +10050) over nine epochs from 2003 November to 2005 April using the VLBI Exploration of Radio Astrometry (VERA) telescope array. We found that the SiO maser distributions around IK Tau are highly variable, depending on the stellar pulsation phase. The velocity structures were complex and also time-variable, and are inconsistent with a simply rotating shell that was suggested by previous observations. Based on fittings of the SiO maser distributions to elliptical ring models, we found that the ring size seems to vary in correlation with the pulsation phase, as previously found for TX Cam. Comparisons of the $v = 1$ and $v = 2$ maser distributions reveal that 42–50% of the maser pairs have a positional offset less than 0.5 mas, suggesting that the maser pumping in these spots is likely to be dominated by line overlapping or collisional pumping, rather than pure radiative pumping. In order to model the velocity structure of the spoke-like features observed in IK Tau, we propose a ballistic-orbit model, in which a gas clump ejected from the stellar surface moves radially outward with a gravitational deceleration, and argue that the stellar mass can be deduced from that model.

Key words: circumstellar matter — masers — stars: AGB and post-AGB — stars: individual (IK Tauri)

1. Introduction

The Asymptotic Giant Branch (AGB) is a specific stage of evolved stars with the initial stellar masses ranging over $0.8\,M_\odot \lesssim M_* \lesssim 8\,M_\odot$. In this stage, a large fraction of stellar mass is ejected from the outer layer of the star into the interstellar medium. This stage involves a physical process that is important for understanding the cycle of material in the universe and star formation in the next generation. Observations of masers in the SiO, H_2O, and OH molecule lines are one of the most effective ways to investigate in detail circumstellar envelopes formed by such copious mass loss. Especially SiO masers exhibit ring-like structures a few times larger than the diameters of the stars, and are located closest to the host stars among the three species of masers (Reid & Moran 1981).

IK Tauri (NML Tau, IRC +10050) is an oxygen-rich Mira variable and is an example of an AGB star that harbors strong SiO maser emission in its circumstellar envelope. The spectral type of IK Tau varies from M8.1 to M11.2 (Olofsson et al. 1998). The pulsation period is about 470 days (Wing & Lockwood 1973; Hale et al. 1997). The distance to IK Tau is estimated to be 250–270 pc (Olofsson et al. 1998; Whitelock et al. 1994). The diameter of the stellar photosphere was

estimated to be 20.2 mas at 2000 January and February by Monnier et al. (2004). This diameter was determined from a uniform disk diameter fit to combined Keck aperture-masking data ($\lambda_0 = 2.257\,\mu$m, $\Delta\lambda = 0.053\,\mu$m) and Infrared Optical Telescope Array (IOTA) data ($\lambda_0 = 2.16\,\mu$m, $\Delta\lambda = 0.32\,\mu$m) in the near infrared.

The SiO ($v = 1$, $J = 1$–0) maser emission in IK Tau was mapped with VLBA once (Boboltz & Diamond 2005). That map shows an elliptical asymmetric ring of the emission extended to an area of approximately 58×32 mas^2, and its major axis is directed northeast–southwest (NE–SW). Line-of-sight velocities of the masers show systematic differences with blue-shifted masers in the NW and red-shifted masers in the SE. Boboltz and Diamond (2005) proposed that the SiO maser shell is rotating around IK Tau. Such asymmetric distributions are also found by previous H_2O/OH maser observations for IK Tau (Lane et al. 1987; Bowers et al. 1993; Yates & Cohen 1994; Marvel et al. 1998; Bains et al. 2003; Bowers et al. 1989). The distributions are elongated in the E–W or SE–NW direction. An accelerating or asymmetric outflow with possible rotation is also suggested by Bains et al. (2003) and Bowers, Claussen, and Johnston (1993). However, because the profiles of SiO masers are highly variable, it is necessary to examine the universality of the rotation/bipolar outflow scenario by monitoring the maser distributions for at least one pulsation period.

In this paper, we present results of our VLBI observations of the SiO ($v = 1$ and $v = 2$, $J = 1$–0) maser transitions toward the Mira variable IK Tau for nine-epochs that covers one pulsation period to investigate the variation of maser structure on the time scale of 510 days. We mainly discuss the global SiO maser distributions for IK Tau. Section 2 describes the observations and data analysis. Section 3 shows the present results. In section 4 we discuss the implications of the observed results.

2. VLBI Observations and Data Analysis

We simultaneously observed two different lines of SiO maser emission ($v = 1$ and $v = 2$, $J = 1$–0) toward IK Tau [RA (J2000.0) = $03^{\rm h}50^{\rm m}43\overset{\rm s}{.}759$, Dec (J2000.0) = $+11°15'31\overset{''}{.}66$] from 2003 November to 2005 May with the VLBI Exploration of Radio Astrometry (VERA). Although VERA is dedicated for maser astrometry using the dual-beam system, only one beam was used for observations presented here, because of the absence of a bright position reference calibrator near IK Tau. In the present observations, therefore, the accurate absolute coordinates of IK Tau cannot be known. Table 1 summarizes these observations. Radio frequencies of 43.122079 GHz and 42.820582 GHz are adopted in this paper as the rest frequencies of SiO $v = 1$ and $v = 2$ transitions, respectively. Clock parameter calibrators 3C 454.3, 0423−013, 0854+201, 4C 13.21, and 4C 39.25 were also observed every 40 minutes. The received signals in the left-hand circular polarization were filtered in two base-band channels (BBCs) with a bandwidth of 16 MHz (equivalent to a velocity width of 111 km s^{-1}). The first BBC was centered at the Doppler-shifted frequency of the $v = 2$, $J = 1$–0 line while the second BBC was automatically placed 304 MHz (= 16 MHz × 19) higher than the first BBC, so that the $v = 1$, $J = 1$–0 line (rest frequency 43.122079 GHz) was also able to be observed (more detail in Iguchi et al. 2005).

The observed signals filtered as mentioned above were recorded with a SONY DIR 1000 recorder at a rate of 128 Mbit s^{-1}. The recorded signals were correlated with the Mitaka FX correlator, which produced auto-correlation and cross-correlation spectra consisting of 512 spectral channels with a frequency spacing of 31.25 kHz, yielding a velocity spacing of 0.22 km s^{-1}.

Visibility calibration was performed using the NRAO AIPS package in a standard manner. The bandpass response was calibrated by using the continuum calibrators. Fringe solutions were obtained by fringe-fitting the visibilities of the strong and compact maser emission in the reference velocity channels for each of the maser transitions (see column 8 of table 1). Because the maser emission in the reference channel had a complicated brightness structure, a map was made using the DIFMAP software package provided by Caltech to obtain a more reliable image used for self-calibration in AIPS. The resulting

Table 1. Summary of the VERA observations.

Epoch	Code* (rYYDDD)	Date	Duration [UT]	Telescope†	1-σ noise ($v = 1, 2$) [mJy beam^{-1}]	Synthesized beam‡	$V_{\rm LSR}$§ ($v = 1, 2$) [km s^{-1}]
1	r03331b	2003/11/26	11:15–18:24	M, R, O, S, N	21, 17	0.7×0.4, −39°	32.2, 33.5
2	r04059a	2004/02/28	04:10–13:00	M, R, O, S	44, 25	0.7×0.4, −43°	31.2, 34,1
3	r04304a	2004/10/30	12:10–21:00	M, R, O	37, 49	0.6×0.6, −82°	30.3, 30.5
4	r04327a	2004/11/22	10:15–19:10	M, R, O, S	33, 23	0.8×0.4, −52°	29.6, 29.6
5	r04359b	2004/12/24	08:15–16:45	M, R, O, S	34, 29	0.7×0.4, −44°	29.8, 29.8
6	r05017a	2005/01/17	06:25–15:55	M, R, O, S	18, 17	0.7×0.4, −41°	30.5, 33.1
7	r05047a	2005/02/16	04:55–13:25	R, O, S	59, 63	0.9×0.5, −5°	34.3, 29.0
8	r05078c	2005/03/19	02:45–11:15	M, R, O, S	24, 24	0.7×0.4, −41°	29.6, 30.2
9	r05111d	2005/04/11	00:45–09:15	M, R, O	29, 29	0.7×0.6, 51°	34.7, 35.2

* Observation code in VERA. YY and DDD shows the year and the day of the year at the observation, respectively.
† Telescope providing valid visibility data. M: VERA telescope at Mizusawa station, R: Iriki, O: Ogasawara, S: Ishigaki, N: The NICT 43 m telescope at Kashima.
‡ Synthesized beam size and position angle in the $v = 1$ SiO maser observation.
§ LSR velocities of the phase- and position-reference channels in $v = 1$ and $v = 2$ maps for each epoch and transition.

self-calibration phase solutions were applied to all channels in each transition. Note that after applying these calibrations, the absolute position information is completely lost from the maser image cubes. The absolute positions of maser spots are not known accurately enough to uniquely register the two different maps of the $v = 1$ and $v = 2$ masers. To measure the intensities of the maser spots and the relative positions of the maser spots with respect to the reference spot, two-dimensional Gaussian functions were fitted with a cut-off signal-to-noise ratio of 8 in each spectral channel using the AIPS task SAD. Note that in this paper, a maser feature indicates a cluster of maser spots that have nearly the same positions and continuous velocity range, as usually defined.

3. Results

Figure 1 shows an optical light curve of IK Tau derived from the American Association of Variable Star Observers (AAVSO) data and SiO maser flux variations obtained with VERA single-dish observation at Iriki station. Epochs of VERA observations presented in this paper are also shown in figure 1 (black triangles). As can be seen in the figure, our observations cover a full pulsation period with a time span of ~ 500 days, and the last seven epochs intensively sample the increasing phase of the light curve ($\phi = 1.6$ to 2.0) with a ~ 1 month interval. The integrated fluxes of the SiO masers around IK Tau show the time-variation correlated with the optical light curve. We note that the light curves of SiO masers are more complicated than that of the optical light, implying that the SiO maser distributions could also drastically vary with the pulsation phase as well as the pulsation cycle.

Figure 2 presents velocity-integrated maps of the $v = 1$ and $v = 2$ maser lines at all nine epochs. Here, we show the spots that have a signal-to-noise ratio larger than 7 in the velocity channel maps. Due to data reduction with self-calibration, the absolute position of the phase center in each image is unknown. To align the two maser maps, we used the relative positions of bright maser spots in the two different maser lines; except for epochs 3 and 9, we found three or four bright maser spots that were detected both in $v = 1$ and $v = 2$ lines, and showed similar distributions. We note that the map registrations obtained here may not be accurate, and could introduce an artificial positional offset. However, as will be discussed later, the relative position error introduced by this method is likely to be smaller than 1 mas (see subsection 4.3 for detail). At epochs 3 and 9, we could not find any set of maser spots that are detected in both $v = 1$ and $v = 2$ maser transitions because there were only a few maser spots in $v = 1$ at epochs 3 and 9 having the same velocity and positions with those in $v = 2$. Thus, the image frames at epochs 3 and 9 were shifted by eye, so that the overall maser distributions of the two transitions coincide with the each other. In figure 2 we also show a stellar disk size of 20.2 mas, which was obtained by interferometric observations in the near-infrared (Monnier et al. 2004).

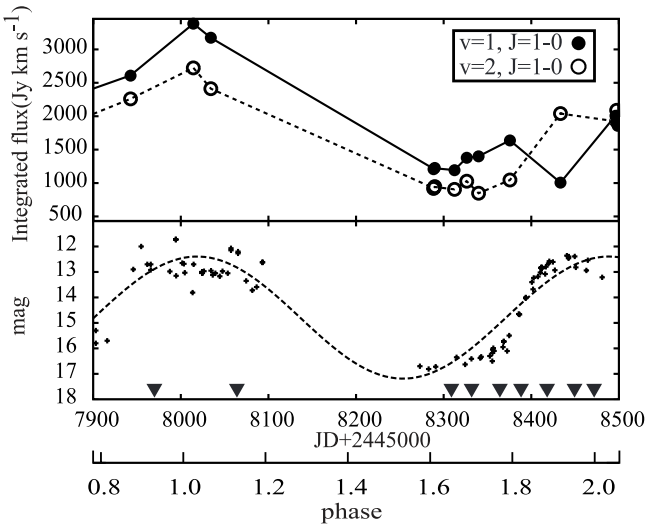

Fig. 1. Top: Time variation of SiO maser flux of IK Tau obtained by VERA single dish observations. Bottom: Visible light curve obtained by AAVSO. Black triangles denote the epochs of the VLBI observation.

The maser spots are distributed at 1.5–2.0 stellar radii, which is typical for SiO masers in Mira variables (e.g., Boboltz & Wittkowski 2005; Cotton et al. 2006). The distributions of $v = 1$ and $v = 2$ masers are basically similar to each other, but maser spots in the $v = 1$ transition tend to be distributed further than those in $v = 2$. Generally, the maser spots show elliptical ring-like or quadrilateral distributions, the most prominent example of which is the one near the light maximum phase (e.g., $\phi = 1.95$ at epoch 8). The position angles of the elongation directions vary depending on time from the NW–SE direction (epochs 1 and 2) to NE–SW (epochs 3 to 9). Although epochs 1 and 8 are almost the same phase as that of the light curve, these maser distributions do not resemble each other. The maser distribution has a clearer ring structure, and there are more maser features at epoch 8 than at epoch 1. The directions of the global elongation are also in disagreement between epoch 1 and epoch 8.

Figure 3 present the flux distributions and the velocity fields in the two lines at the different light-curve phases ($\phi = 0.93$ to 2.00). The maser parameters were obtained with the AIPS task SAD with a cut-off signal-to-noise ratio of 8 (rather than 7 used for figure 2); in the task SAD, the cutoff S/N of 7 was not high enough to avoid noise contamination. Hence, in figure 3 the number of maser spots is slightly smaller than that in figure 2 due to the cut-off S/N difference. Each upper sub-panel of figure 3 shows the flux density of the maser spots against the local-standard-of-rest (LSR) velocity. The flux densities of the cross-power spectra observed with the VERA baselines are about 1/20 of those found in the total-power spectra. We find that the blue-shifted masers have higher flux densities than the red-shifted masers, being similar to the flux density distribution found by Boboltz and Diamond (2005). Although blue-shifted and red-shifted maser features showed a clear spatial separation in the map obtained by Boboltz and Diamond (2005), the maser features observed in the present paper exhibit a mixed spatial distribution, indicating that a simple rotating shell is not enough to reproduce the observed velocity structure (see next section for detail).

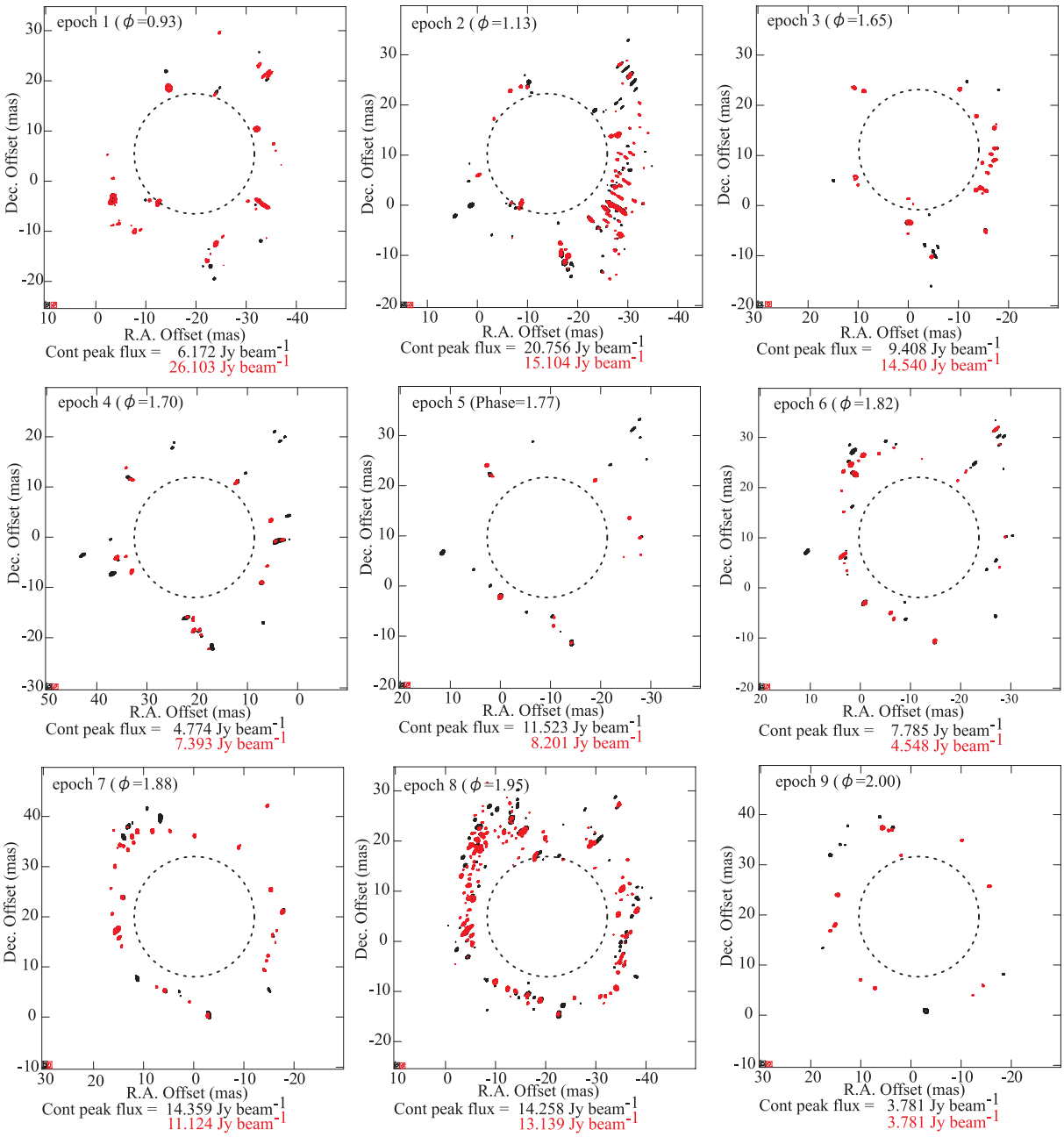

Fig. 2. Intensity maps of the SiO ($v = 1$ and $v = 2$, $J = 1$–0) maser emission toward IK Tau, obtained by integrating the emission over all velocity channels. The $v = 1$ map (black contour) is superposed on the $v = 2$ map (red contour). The contour levels are set to 1, 1.6, 2.6, 4.1, 6.6, 10.5, 16.8, 26.8, 42.9, and 68.7% of the peak integrated flux in each panel. Ellipses at the left-bottom corner of each sub panel indicate the synthesized beam of the $v = 1$ and $v = 2$ maps. The dashed circle represents a stellar disk diameter of 20.2 mas from Monnier et al. (2004). The location of the stellar disk is conjecture.

4. Discussion

4.1. *Velocity Structure and Relation between SiO/H_2O/OH Masers in IK Tau*

In the present SiO maser observations, the velocity structure changed greatly with time, and the distributions of the blue-shifted and red-shifted masers were more complicated than that found by Boboltz and Diamond (2005), even at the same stellar phase. Here, we calculated the flux-weighted average radial velocities of the maser spots in 8 sectors around the star based on a method by Cotton et al. (2004). In this calculation, the maser spots shown in figure 3 were used. The resultant sector velocities do not show any clear trend concerning the velocity structure, and the sector velocities changed from epoch to epoch within a few km s^{-1}. This indicates that the velocity structure in the outer stellar atmosphere is dominated by turbulence rather than systemic motion, such as stellar rotation. Such turbulent motions will tend to mask the signature of systematic rotation, because the host star must be a slow rotator due to its enormous size.

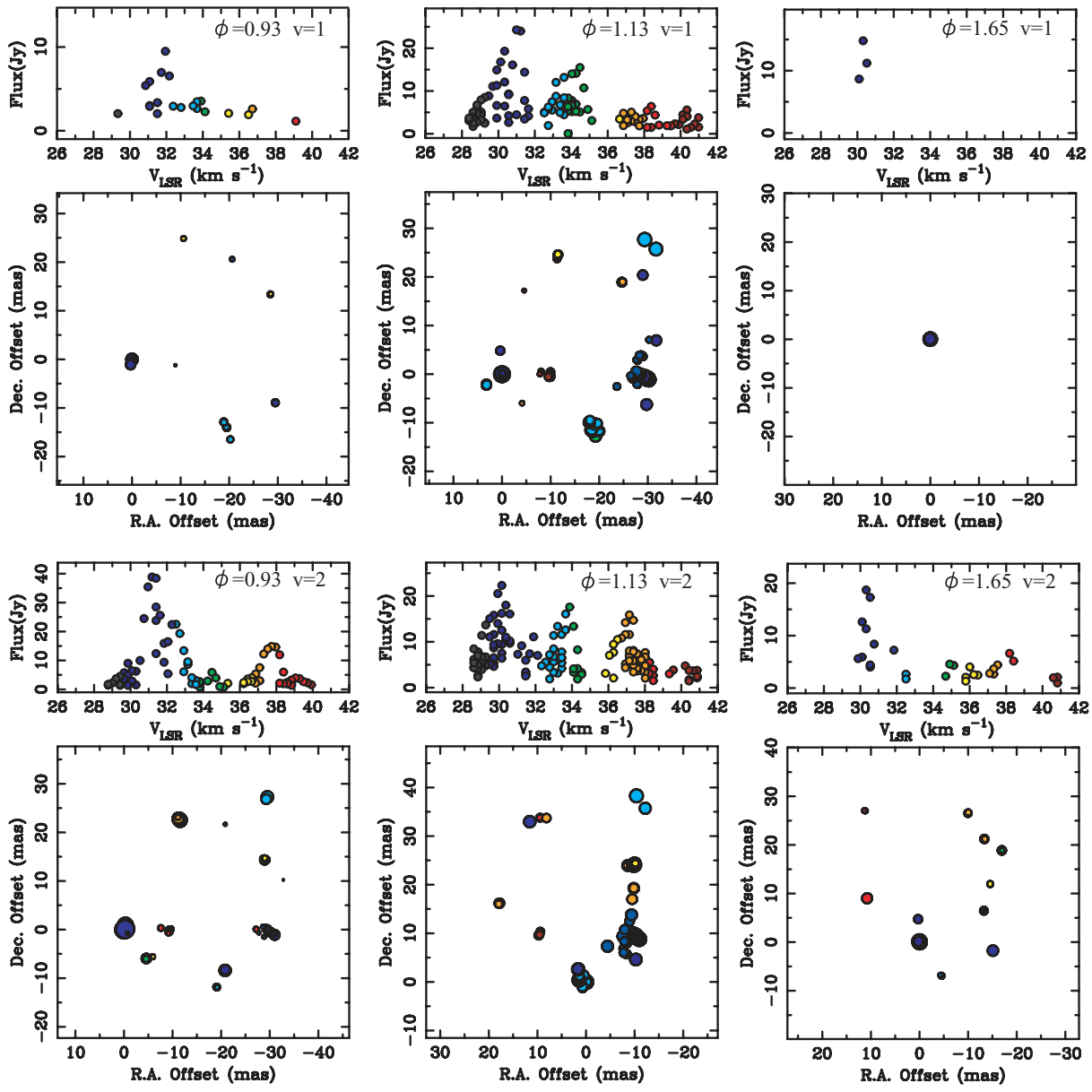

Fig. 3. Local-standard-of-rest (LSR) velocity distribution of SiO $v = 1$ (top) and $v = 2$ (bottom) $J = 1$–0 maser of IK Tau. The small sub-panel shows the correlated flux density against the LSR velocity. The large sub-panel plots distributions of maser features in the map, and the size of the plotted circles are proportional to the logarithm of the feature flux density. The errors in the positions of the features are smaller than the circle sizes. Color-codes represent the LSR velocity in both sub-panels.

In order to reduce the effect of these turbulent motions, and to investigate if there is a systemic velocity structure, such as stellar rotation, we averaged the sector velocities over nine epochs. Figure 4 shows the sector velocities averaged over the nine epochs for the SiO masers in IK Tau (sector's opening angle is 45°). The velocity variation through the sectors can be fitted by a sinusoidal curve ($\chi^2 = 0.52$) or by a straight ($\chi^2 = 0.81$) line. Since there is no significant difference in χ^2 for a sinusoidal fit and a constant velocity fit, our results do not provide any direct evidence for a rotational SiO maser shell, which was proposed by Boboltz and Diamond (2005). Even if we adopt the sinusoidal fitting, the sector velocity structure implies rotation with a velocity of $\sim 0.94\,\mathrm{km\,s^{-1}}$ and a rotation axis at a position angle of $\sim 227°$, which is nearly opposite to the rotation axis obtained by Boboltz and Diamond (2005) ($\sim 59°$). In fact, the blue-shifted and red-shifted components in the present maser maps are located in the opposite sides when compared to the results of Boboltz and Diamond (2005). Also, in Boboltz and Diamond (2005), the blue-shifted and red-shifted components were clearly distinguished like other stars such as NML Cyg (Boboltz & Marvel 2000) and R Aqr (Hollis et al. 2001; Cotton et al. 2004, 2006), suggesting the rotation of SiO maser shells. However, our maser maps do not clearly show any systematic velocity structure in each epoch. Therefore, the apparent rotation-like structure reported in Boboltz and Diamond (2005) is not permanent, and was

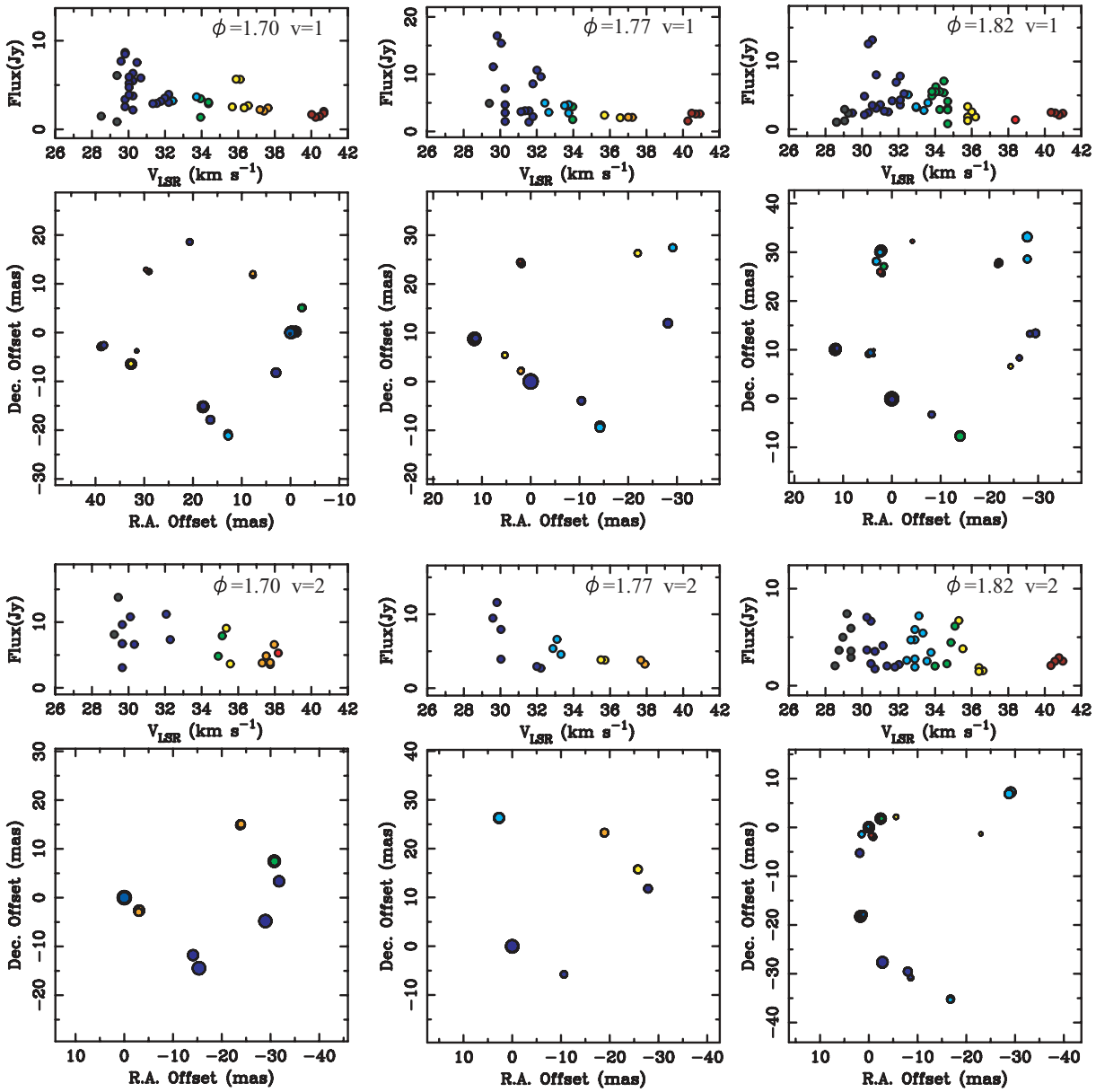

Fig. 3. (Continued)

probably made by chance.

Although the spatial maser distributions in 2005 (obtained with VERA) resemble the structure in 1996 (Boboltz & Diamond 2005) in terms of an elongation axis in the SW–NE direction, the major axis of the elongation in 1996 was about 1.5-times larger than in 2005. We also note that during our observations the direction of the elongation axis changed between the first two epochs and the remaining seven epochs. Hence, the elliptical ring/quadrilateral distributions are not permanently stable, and are varying with time, possibly in relation to the stellar pulsation phase. The systematic velocity structure seen in Boboltz and Diamond (2005) may be due to an expanding (or contracting) shell, in which expansion (or contraction) motion projected on the line of sight caused the systematic velocity structure, which is apparently indistinguishable from a stellar rotation. A non-radial mode of the stellar pulsation may explain these characteristics of the SiO maser distributions around IK Tau, including their time variations.

Other molecular masers such as H_2O and OH masers, also show elongated distributions in the SW–NE direction. For an H_2O maser, Bowers et al. (1993) suggested that the H_2O maser shell has an accelerating and asymmetric outflow with a possible rotation based on the distance–radial velocity ($\theta - V$) diagrams. Bains et al. (2003) found that faint H_2O maser clumps that are distributed over an elliptical region of ~ 200 mas $\times \sim 100$ mas show a systematic velocity gradient, with blue-shifted clumps in the east and red-shifted clumps in the west, which can be explained by a rotation of the H_2O maser shell. Bowers et al. (1989) obtained a distribution and

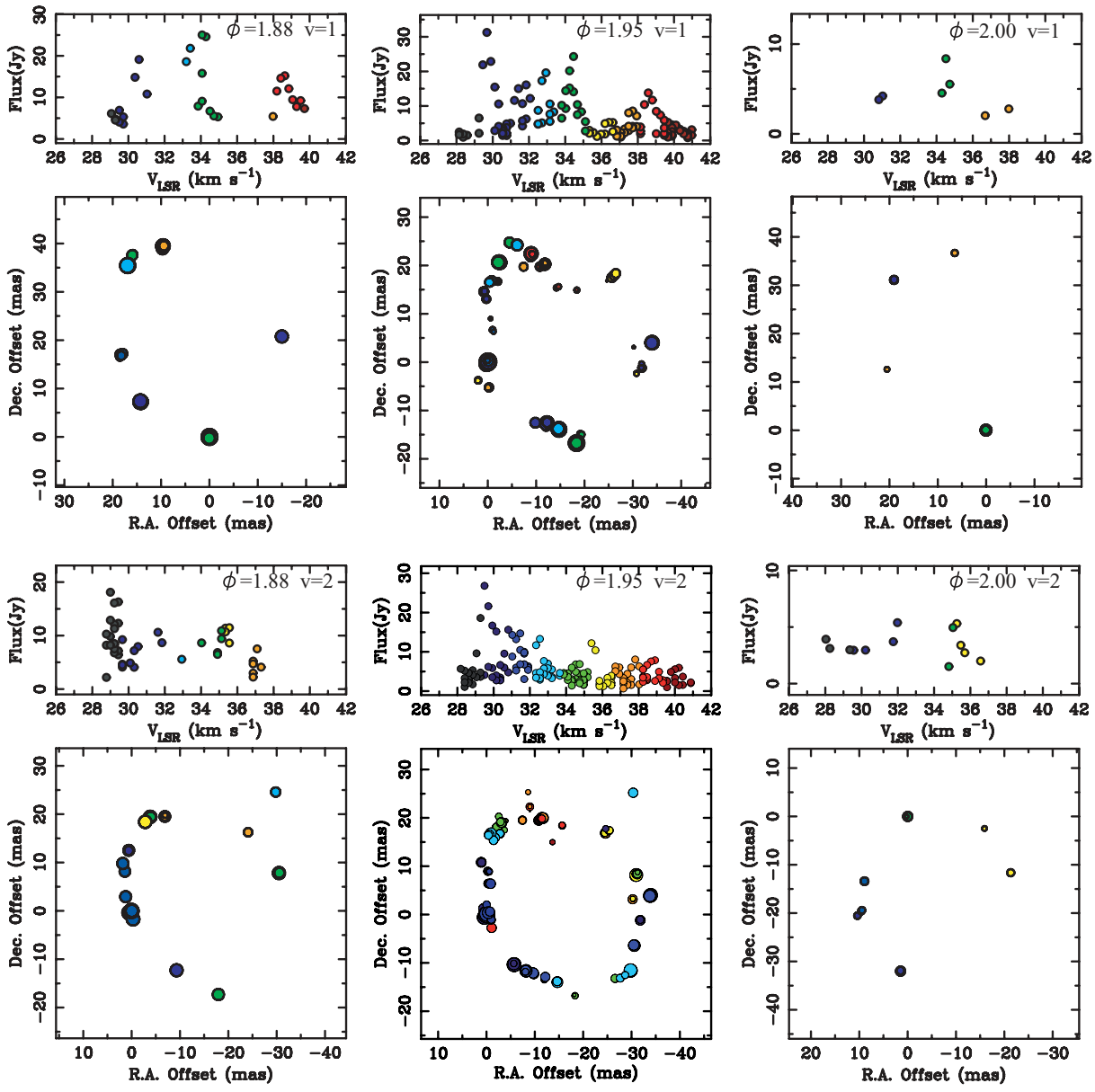

Fig. 3. (Continued)

velocity structure of OH maser similar to that of H_2O maser. However, as we have already shown, the SiO velocity structure is not permanent, but varies with the pulsation phase. Therefore, one cannot rule out the possibility that the velocity structures of the H_2O and OH masers also vary with time. In that case, the systematic velocity gradient of the H_2O and OH masers may not be due to permanent rotation. For further conclusions, some additional information (such as intensive multi-epoch monitoring of the H_2O and OH masers) is necessary.

Measuring the proper motions of maser spots is another approach to understanding the velocity structure of circumstellar regions traced with masers. Based on the same method as that of Boboltz et al. (1997), we tried to measure the proper motions of SiO masers between two or three epochs, which were sampled with an $\sim$1 month interval. However, reliable proper motions were detected for only a few spots, mainly due to a drastic variation of the maser distributions between epochs, as can be seen in figure 2. Thus, for the proper motion measurements, an observational interval shorter than 1 month is preferable for a reliable identification of SiO maser spots.

4.2. *Time Variation of the Ring Structure*

Here, we discuss the size variation of the maser distribution area, depending on the stellar pulsation phase using elliptical ring models. We approximate the maser distributions with an elliptical ring, which is described as a circular ring with a ring radius of r and a ring width of Δr projected onto the sky plane with an inclination angle of θ. First, the ring center position was searched by finding the location of an annulus that contains the maximum logarithmic flux (an annulus width was set to be 0.1 mas). After the ring center determination, the

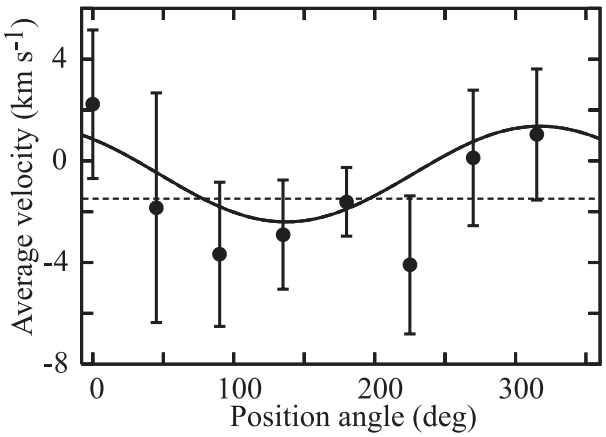

Fig. 4. Sector velocities averaged over the nine epochs and the two maser transitions. The uncertainty of the average velocity was calculated from the intensity-weighted standard deviation of the feature velocities.

inclination (θ) was estimated by finding the parameter that provides the largest logarithmic flux density in an elliptic annulus. Then, the ring radius, r, was determined so that the logarithmic flux enclosed within the projected ellipse becomes 50% of the total logarithmic intensity. The ring width Δr was also determined as $\Delta r = r_{\rm out} - r_{\rm in}$, where $r_{\rm in}$ and $r_{\rm out}$ are inner and outer radii, which are defined so that the enclosed logarithmic fluxes within the ellipses become 25% and 75% of the total logarithmic intensity, respectively. We note that this procedure is similar to that of Yi et al. (2005).

The obtained ring radii and widths at each epoch are given in table 2, and the time variation of the ring radii with the light curve phase is plotted in figure 5. Note that in figure 5 vertical bars show the ring widths, Δr. During $\phi = 1.65$–2.00, the $v = 1$ and $v = 2$ ring radii seemed to gradually increase with the phase. In fact, while plots for $v = 1$ can be fitted by a sinusoidal curve or a constant line ($\chi^2_{v=1} = 0.66$ for sinusoidal curve and $\chi^2_{v=1} = 0.94$ for constant), the plot for $v = 2$ is better represented by a sinusoidal curve ($\chi^2_{v=2} = 1.07$ for sinusoidal curve and $\chi^2_{v=2} = 4.94$ for constant line), indicating that there is a ring size variation with the pulsation phase (note that in χ^2 calculations, the ring width Δr is assumed to represent the error of the ring size, r). In figure 5, sinusoidal fits to both $v = 1$ and $v = 2$ ring sizes are also shown. The results of the sinusoidal fits indicate that the radius of $v = 2$ is about 1 mas smaller than that of $v = 1$.

For IK Tau, the maser distribution found by Boboltz and Diamond (2005) ($58 \times 32\,\mathrm{mas}^2$) was more widely spread than those in the present results at all phases (see table 2), although these observations were made at almost the same phase ($\phi = 0.85/0.82$ and 0.85, respectively). These results indicate that the maser distributions vary with stellar pulsation cycles. SiO maser ring-size variations were also intensively observed for TX Cam (Diamond & Kemball 2003; Gonidakis et al. 2006). Here, we focus on the ring-size behavior of TX Cam at the pulsation phase $\phi = 0.6$–$1.0 + n$ (where n is the integer corresponding to stellar pulsation cycles) to compare with the densely-sampled phase of IK Tau in our observations.

Table 2. Parameters for circular ring model obtained with IRING.

Epoch	Phase ϕ	PA* (°)	$\theta^\dagger$ (°)	$r^\ddagger$ (mas)	$\Delta r^\S$ (mas)
SiO ($J = 1$–0, $v = 1$) line					
1	0.93	99	21	16.9	1.7
2	1.13	147	17	16.4	5.6
3	1.65	20	8	12.1	5.2
4	1.70	80	4	15.0	5.9
5	1.77	50	16	16.5	5.6
6	1.82	0	0	19.4	4.7
7	1.88	70	8	18.1	4.5
8	1.95	59	21	18.0	3.7
9	2.00	94	23	18.5	0.8
SiO ($J = 1$–0, $v = 2$) line					
1	0.93	57	29	16.5	3.5
2	1.13	83	15	16.1	1.7
3	1.65	124	2	13.4	1.0
4	1.70	80	8	14.1	2.3
5	1.77	30	7	16.5	4.8
6	1.82	20	3	18.6	1.8
7	1.88	45	10	16.2	4.7
8	1.95	71	21	17.0	2.9
9	2.00	165	5	16.9	1.3

* Position angle receding major axis, east from north.
† Inclination of the axis perpendicular to the ring plane from the sky plane.
‡ Length of semimajor axis.
§ Width between the inner and outer sides of the ring.

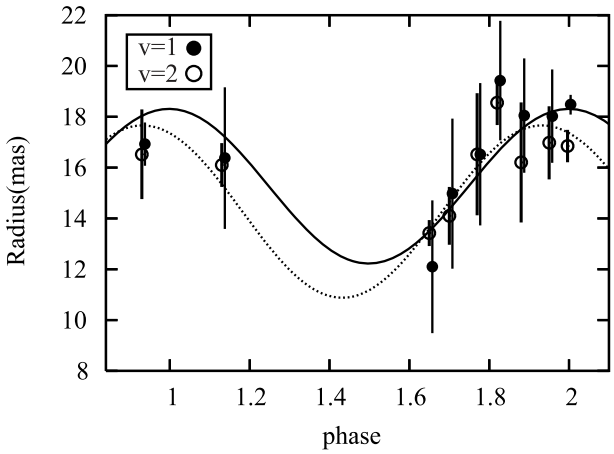

Fig. 5. Ring radius variations of SiO ($v = 1$ and $v = 2$, $J = 1$–0) emission calculated by using IRING (table 2). The horizontal axis is the light-curve phase of IK Tau. The solid and dashed curves show sinusoidal fits for the $v = 1$ and $v = 2$ ring radii, respectively. A vertical bar represents the ring width, Δr.

Diamond and Kemball (2003) revealed that the ring size of SiO masers in TX Cam is increasing in that phase. Gonidakis, Diamond, and Kemball (2006) presented the SiO ring-variation for a longer period (nearly 2 stellar cycles), and showed that the ring size at $\phi = 1.6$–2.0 (one stellar cycle later than that of

Diamond & Kemball 2003) also has an increasing trend with time, although the expansion velocity is fairly smaller than that observed in Diamond and Kemball (2003). These results indicate that both IK Tau and TX Cam have the same trend in the ring-size variations, at least at the stellar phase of $\phi = 0.6$–1.0. Regarding other Mira variables, Cotton et al. (2004) and Cotton et al. (2006) presented the time variation of the SiO ring for U Her, R Aqr, *o* Cet, R Leo, and S CrB. Although the sampling was not dense enough (typically a few epochs per one stellar pulsation cycle) to compare them with our results, the ring size of R Leo may indicate an increasing trend at the stellar phase of $\phi = 0.6$–1.0, being similar to IK Tau and TX Cam. In that phase, S CrB may also have the same trend. For other sources, the ring sizes of U Her, R Aqr, and *o* Cet seem to be stable, or even slightly decreasing, in the case of *o* Cet. These different trends of the ring-size variation may originate from the characteristics of individual stars, or a variation of stellar properties, depending on the stellar pulsation cycle.

These different trends in the ring size variations may be explained in terms of the expansion velocity of the shell and the escape velocity of the star (Gonidakis et al. 2006), i.e., if the shell is gravitationally bound, the shell exhibits both expansions and contractions, and if the shell is unbound, the shell should permanently expand. In the present observations of IK Tau, the expansion velocity does not seem to exceed the escape velocity. Here, we estimated the expansion velocities by time-differentiation of the sinusoidal curve shown in figure 5. The expansion velocities of the $v = 1$ maser ring was found to be -0.3 to 14.4 km s^{-1} at $\phi = 1.65$–2.00, and to be -8.6 to 19.5 km s^{-1} for the $v = 2$ maser ring at the same phase. On the other hand, the escape velocities are 20.1 to 22.9 km s^{-1} for $v = 1$ maser ring and 16.7 to 23.0 km s^{-1} for $v = 2$ maser ring, respectively (here we assume a stellar mass of $1\,M_{\odot}$ and a distance of 250 pc). Thus in the case of IK Tau, maser shells are likely to be bound, and contraction may be possibly seen if the whole stellar pulsation cycle is densely sampled. Non-detection of contraction may be due to relatively sparse sampling of the monitoring epochs at the contraction phase. In fact, in case of TX Cam there exist maser components that are moving inwards showing a contraction of the ring in the second cycle, although the contraction was not seen in the first cycle (Gonidakis et al. 2006). Gonidakis, Diamond, and Kemball (2006) mentioned that the expansion velocities of the masers seen in the first cycle are larger than the escape velocity, which can explain the lack of contraction. For a further understanding of shell size variation, accurate determinations of the escape velocity (i.e., stellar mass) as well as the expansion velocity (i.e., proper motion measurements) will be necessary, and this is an issue to be studied in the near future.

4.3. Relative Position between v = 1 and v = 2 Maser Spots

In this subsection we discuss the relative position difference of SiO masers in a $v = 1$ and $v = 2$ map. Since epoch 2 ($\phi = 1.13$) and epoch 8 ($\phi = 1.95$) are near the maser intensity maximum, and there are enough maser spots for statistics, we consider epoch 2 and epoch 8 for comparisons of the $v = 1$ and $v = 2$ spot positions. Figure 6 shows the number distribution of the angular distances from each $v = 1$ spot to the nearest $v = 2$ spot having a radial velocity within ± 0.22 km s^{-1} ($= \pm 1$ ch) of that of the $v = 1$ spot. To investigate the spot separation between the $v = 1$ and $v = 2$ maser spots, one needs a relative registration of the two maps. For epoch 2, we used the spot at $V_{\rm LSR} = 41.2$ km s^{-1} for $v = 1$ and $V_{\rm LSR} = 41.1$ km s^{-1} for $v = 2$ as a reference maser spot, which were assumed to be emitted from the same gas clump. For epoch 8, we used $V_{\rm LSR} = 29.7$ km s^{-1} for $v = 1$ and 29.5 km s^{-1} for $v = 2$ as a reference spot. These reference spots are bright, and also have simple structures both in the $v = 1$ and $v = 2$ maser lines. Figure 6 shows that there is a sharp peak in the distributions of the angular separations between the $v = 1$ and $v = 2$ spot pair at $D \sim 0$ mas, indicating that the overall distributions of the $v = 1$ and $v = 2$ maser spots are similar to each other. In fact, 42% and 50% of the maser pair of the $v = 1$ and $v = 2$ spots have an angular distance of less than 0.5 mas at epoch 2 and epoch 8, respectively. Note that the spot pair with angular distances greater than a few tens of mas are virtually independent spots, because a few tens of mas corresponds to the scale of the SiO maser rings. Note that the above results depend on the accuracy of the reference spot positions, and hence we should carefully consider the effect of the offsets that could be introduced by any mis-identification of the reference spots. To evaluate this, in the right panels of figure 6 we show the number distribution of the maser pairs of the $v = 1$ and $v = 2$ spots with the angular distance being less than 0.5 mas with varying position offsets between the $v = 1$ and $v = 2$ maps, both in the X and Y directions. As can be seen in figure 6, the number of pairs is strongly peaked at the initial reference position obtained by using the reference spots described above, and the number of pairs drastically decreases if one adopts a 1 mas offset in both dX and dY. These results suggest that the accuracy of the map registration obtained with the reference spots is about 1 mas, or better.

We now discuss the SiO maser pumping mechanism based on the relative positions of the maser spots obtained above. There exist two major theoretical models of the SiO maser pumping mechanism, namely, radiative pumping (e.g., Desmurs et al. 2000; Bujarrabal et al. 1996; Bujarrabal 1996, 1994a, 1994b) and collisional pumping (e.g., Lockett & Elitzur 1992; Doel et al. 1995). In the radiative pumping model, the energy of the maser pumping comes from the stellar radiation at 8 μm, which corresponds to $\Delta v = 1$ ro-vibrational SiO transitions. Generally, the radiative pumping model expects that the distributions of the maser spots in the two transitions do not spatially coincide with each other due to the large energy difference in the two vibrational levels ($\Delta E/k \approx 1800$ K). It is also possible that radiative processes tend to quench the $v = 1$ maser lines when the opacities are high enough to invert the $v = 2$ lines. In contrast, in the collisional model the shock in the mass-loss outflow provides the maser pump energy by means of collisions with the H_2 molecules, and thus the collisional pumping model predicts the same locations of the $v = 1$ and $v = 2$ maser spots in the shock region. In our observations of IK Tau, figures 2 and 6 show that a large fraction of pairs of the $v = 1$ and $v = 2$ spots are located within ~ 1 mas from each other. This trend favors the collisional pumping mechanism, rather than the pure radiative pumping mechanism. However, there is another radiative pumping model that predicts close locations of the $v = 1$ and $v = 2$ maser lines, which is called

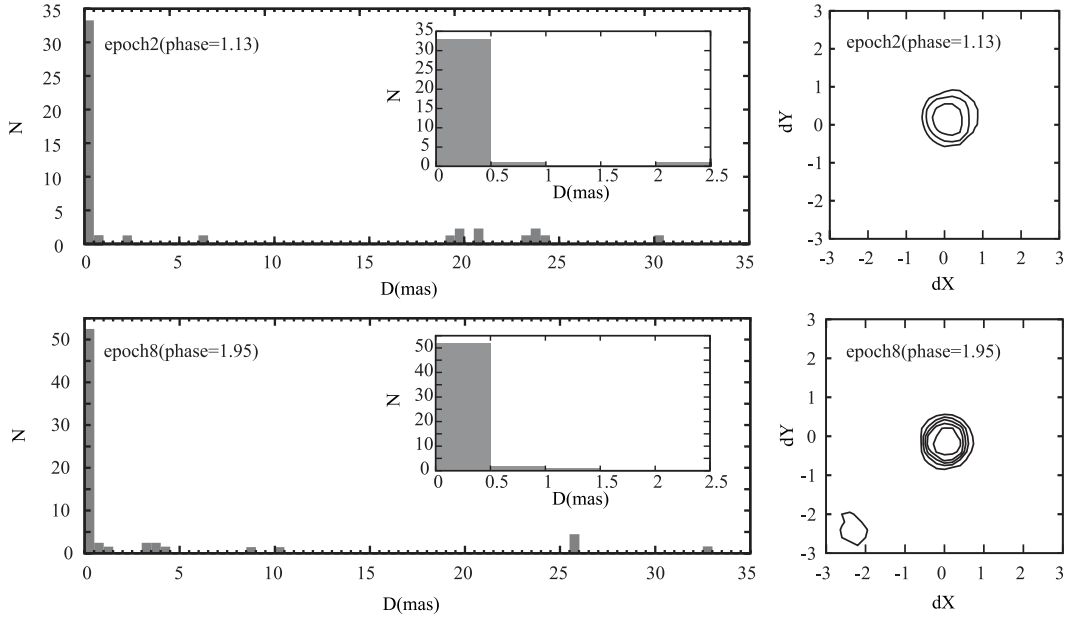

Fig. 6. Left: Number distribution of the angular distances from each $v = 1$ spot to the nearest $v = 2$ spot at nearly same radial velocity (within $\pm 0.22\,\mathrm{km\,s^{-1}}$). The data displayed in figure 3 are used. Center: Zoom-in view of left panel around a small D value. Right: The number distribution of $v = 1$ and $v = 2$ maser pairs with the angular distance less 0.5 mas, with varying relative offsets in X and Y coordinates between $v = 1$ and $v = 2$ maps. One contour level corresponds to 10 pairs of $v = 1$ and $v = 2$ masers.

the line-overlapping model (e.g., Bujarrabal et al. 1996; Soria-Ruiz et al. 2004). In this model, the line-overlapping between the transition of H_2O molecules and the $\Delta v = 1$ ro-vibrational transition of SiO molecules at 8 μm plays a major role in population inversion of the SiO transitions. In this model, the infrared photons from the H_2O $\nu_2 = 0$ 12_{75} to $\nu_1 = 1$ 11_{66} transition excites the SiO $v = 2$ $J = 1$ from $v = 1$ $J = 0$, and hence population inversion can occur at both the $v = 2$ and $v = 1$ $J = 1$–0 transition in the same gas, resulting in the same location of the $v = 1$ and $v = 2$ maser spots. The line-overlapping model can also explain the close locations of the $v = 1$ and $v = 2$ maser spots in IK Tau, and thus cannot be ruled out by our observations. Also, we note that in the NE region of epochs 6 and 7, there are only a few pairs of $v = 1$ and $v = 2$ spots that have the same radial velocity and positions, and the $v = 2$ maser features are located relatively closer to the star than the $v = 1$ masers (see figures 2 and 3). This may suggest that radiative pumping occurs at least in that region. Probably the maser pumping is not merely caused by one of above processes, but is likely to be more complicated as a combination of these processes. In fact, Doel et al. (1995) indicate that the SiO pumping mechanism could be a combination of collisional and radiative events. In the future, 2-beam phase-referencing observations with VERA and precise astrometry better than 1 mas would be helpful for better understanding the SiO pumping mechanism. For instance, Kamohara et al. (2008) have compared the maser spots of $v = 1$ and $v = 2$ in R Aqr with an accuracy of ~ 0.3 mas using VERA 2-beam observational data. In addition to such observations, pumping models that address the degree of spot coincidence between the $v = 1$ and $v = 2$ SiO maser lines will be required for further understanding this issue.

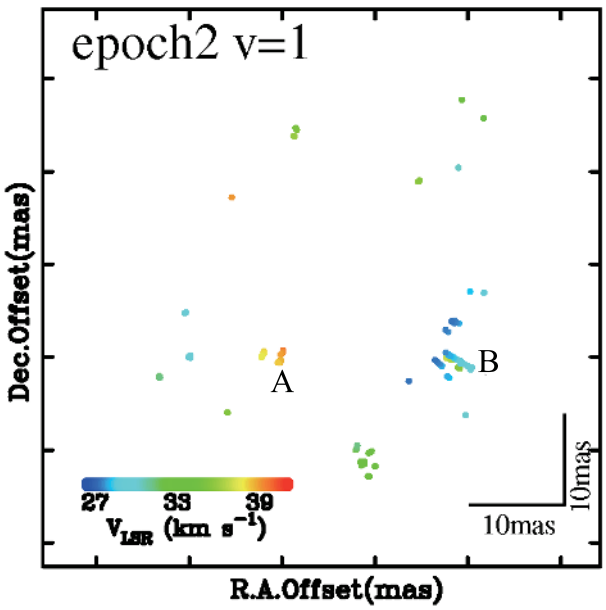

Fig. 7. Example of locations and internal structures of spoke-like features (A and B). The LSR velocity of maser spots are color-coded. (Same as figure 3, but the circle size is set to be constant regardless of the maser flux to clearly show spoke-like structure.)

4.4. *Spoke-Like Maser Features and a Ballistic-Orbit Model*

In IK Tau there are spoke-like (or radially extended) maser features. Remarkable examples of such spokes are found at epochs 1, 2, and 8 (see figures 2 and 3). In figure 7, we show examples of spokes obtained at epoch 2 for the $v = 1$

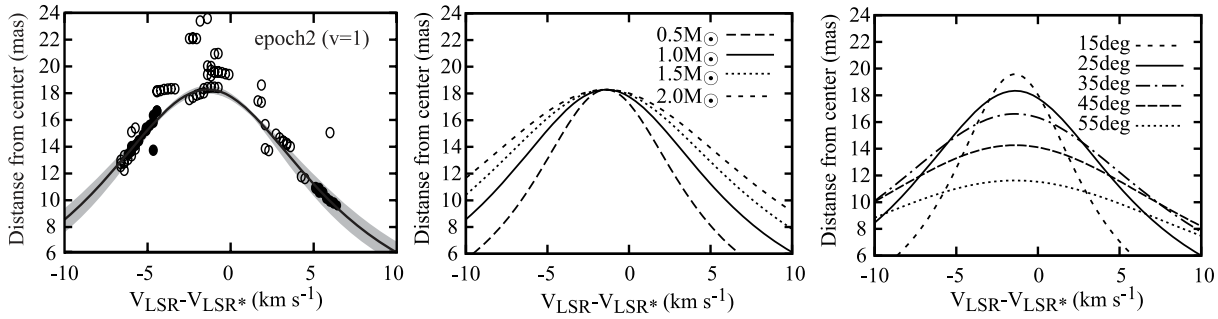

Fig. 8. Left: Fitted ballistic orbit (solid line) for the spoke-like features (black circle) in the distance–velocity diagram of SiO ($J = 1$–0, $v = 1$) at epoch 2. The fitting parameters: $M = 1 M_{\odot}$, $r_0 = 7.6 \times 10^{11}$ m ($\sim$20 mas at 250 pc), and $i = 26°$. The gray zone shows the area of uncertainty coming from the stellar mass of $M = 1.0 \pm 0.1\, M_{\odot}$ and the inclination of $i = 26° \pm 2°$. Center: The dependence of the ballistic orbit curve on the stellar mass. The other parameters are fixed to be $r_0 = 7.6 \times 10^{11}$ m and $i = 26°$. Right: Dependence of the ballistic orbit curve on the inclination angle. The other parameters are fixed to be $M = 1.0\, M_{\odot}$ and $r_0 = 7.6 \times 10^{11}$ m.

masers (e.g., the features labeled as A and B). Mostly, spokes are blue-shifted with respect to the LSR velocity of the star, although there are a few red-shifted features that also exhibit short spoke-like structure. These spoke-like features have velocity gradients, whose radial velocities are approaching the systemic velocity with increasing distance from the star. These spoke-like structures are also seen in TX Cam (Yi et al. 2005), *o* Cet (Cotton et al. 2006, 2008), R Leo (Cotton et al. 2008), U Her (Cotton et al. 2008), and OH 26.25+0.6 (Cotton et al. 2008). Cotton et al. (2006) showed that the magnetic field in the spoke-like features is elongated with the spoke structure. They argued that the spoke-like features reflect the dynamical motion in the envelope rather than parts of the global rotation of the envelope. Yi et al. (2005) suggested that the spoke-like structure traces a part of the entire circumstellar shell, which has a decreasing radial velocity with increasing the distance from the star.

Here we propose a ballistic-orbit model that describes the decelerating velocity structure in the spoke. Suppose that a spoke comprises of a radially aligned ensemble of point masses, which were continuously ejected from the surface of the star. We assume that the individual features are moving in a radial direction with deceleration due to the stellar gravity. Then, the equation of motion for a maser spot in a spoke is written as

$$dv/dt = -GM/r^2, \tag{1}$$

where $v = dr/dt$. Here, r is the distance from the center of the host star, v the radial velocity ($V_{\rm LSR} - V^*_{\rm LSR}$) at r, G the gravitational constant, and M the stellar mass.
Since $dt = dr/v$, we obtain

$$vdv = -GM/r^2 dr. \tag{2}$$

By integrating equation (2), we obtain

$$\frac{r}{r_0} = \frac{1}{1 + v^2/v_0^2}, \tag{3}$$

where $v_0^2 = 2GM/r_0$. Here, the integral constant is determined so that the velocity v vanishes at the apocenter, $r = r_0$. In practice, the spoke-like maser feature is projected onto the celestial sphere with an inclination angle i. Using a sky-projected distance to a maser spot from the star, $r' = r\cos i$ and a radial velocity of the spot, $v' = v \sin i$, equation (3) may be written as

$$r' = \frac{v_0^2 r_0 \cos i \sin^2 i}{v_0^2 \sin^2 i + v'^2}, \tag{4}$$

which provides a relation between the direct observables, such as the projected distance from the star, r', and radial velocity, v'.

Figure 8 shows an example of the velocity structure of the spoke-like features modeled with the above equations. Here, we used the two prominent spokes at epoch 2 for $v = 1$ maser (features A and B in figure 7), since they have a large velocity range as well as a large radial extent. Figure 8 demonstrates that the velocity structure of the spoke-like features is well fitted by the velocity curve expected from the ballistic orbit model [equation (4)] with typical values of r_0, M, and i ($r_0 = 7.6 \times 10^{11}$ m, $M = 1.0\, M_{\odot}$, and $i = 26°$). In the right panels of figure 8 we also show velocity curves for different stellar masses (M) and inclinations (i), respectively. Since the shape of the velocity curve is strongly dependent on the parameters, such as M and i, we can constrain these parameters fairly well by the ballistic-orbit model. In fact, the fitting of the velocity curve of the two spoke-like features provides a stellar mass of $1.0 \pm 0.1\, M_{\odot}$ and an inclination of $26° \pm 2°$. From these parameters and equation (4), the ejection velocity at a stellar surface of $R_{\rm surf} = 10.1$ mas is also calculated to be $v_{\rm surf} = 11.6\,{\rm km\,s^{-1}}$. This ejection velocity is less than the escape velocity at the stellar surface, which is estimated to be $26.6\,{\rm km\,s^{-1}}$. This is consistent with the picture that the SiO shell expansion velocity is smaller than the escape velocity of the star, as was discussed in subsection 4.2. We note that in figure 8 other spoke-like features as well as non-spoke-like maser features are also distributed along the model curve. Hence, the present model may explain the overall velocity structures in the SiO maser shell simply by the stellar gravity. Applications of this method to other stars will be important to see if the ballistic-orbit model generally explains the properties of SiO maser spokes, and if it turns out to work well it will provide a rather new and unique tool to investigate the mass of AGB stars.

We are grateful to the referee, Dr. V. Bujarrabal, for careful reading of the manuscript and fruitful suggestions. We also

appreciate Dr. D. A. Boboltz for his careful reading and his invaluable comments. We also acknowledge the AAVSO International Database contributed by worldwide variable-star observers. We would also like to thank all the VERA staffs and students who have supported the array operation and the data correlation. T.O/H.I. and H. I. have been financially supported by Grants-in-Aid for Scientific Research from Japan Society for the Promotion Science (17340055 and 18740109).

References

Bains, I., Cohen, R. J., Louridas, A., Richards, A. M. S., Rosa-González, D., & Yates, J. A. 2003, MNRAS, 342, 8
Boboltz, D. A., & Diamond, P. J. 2005, ApJ, 625, 978
Boboltz, D. A., Diamond, P. J., & Kemball, A. J. 1997, ApJ, 487, L147
Boboltz, D. A., & Marvel, K. B. 2000, ApJ, 545, L149
Boboltz, D. A., & Wittkowski, M. 2005, ApJ, 618, 953
Bowers, P. F., Claussen, M. J., & Johnston, K. J. 1993, AJ, 105, 284
Bowers, P. F., Johnston, K. J., & de Vegt, C. 1989, ApJ, 340, 479
Bujarrabal, V. 1994a, A&A, 285, 953
Bujarrabal, V. 1994b, A&A, 285, 971
Bujarrabal, V., Alcolea, J., Sánchez Contreras, C., & Colomer, F. 1996, A&A, 314, 883
Chen, X., Shen, Z.-Q, Imai, H., & Kamohara, R. 2006, ApJ, 640, 982
Chen, X., Shen, Z.-Q, & Xu, Y. 2007, ChJA&A, 7, 531
Cotton, W. D., et al. 2004, A&A, 414, 275
Cotton, W. D., et al. 2006, A&A, 456, 339
Cotton, W. D., Perrin, G., & Lopez, B. 2008, A&A, 477, 853
Desmurs, J. F., Bujarrabal, V., Colomer, F., & Alcolea, J. 2000, A&A, 360, 189
Diamond, P. J., & Kemball, A. J. 2003, ApJ, 599, 1372
Doel, R. C., Gray, M. D., Humphreys, E. M. L., Braithwaite, M. F., & Field, D. 1995, A&A. 302, 797
Gonidakis, I., Diamond, P. J., & Kemball, A. J. 2006 AIP Conf. Proc., 848, 333
Hale, D. D. S., et al. 1997, ApJ, 490, 407
Hollis, J. M., Boboltz, D. A., Pedelty, J. A., White, S. M., & Forster, J. R. 2001, ApJ, 559, L37
Iguchi, S., Kurayama, T., Kawaguchi, N., & Kawakami, K. 2005, PASJ, 57, 259
Kamohara, R, et al. 2008, PASJ, 60, 1023
Lane, A. P., Johnston, K. J., Bowers, P. F., Spencer, J. H., & Diamond, P. J. 1987, ApJ, 323, 756
Lockett, P., & Elitzur, M. 1992, ApJ, 399, 704
Marvel, K. B., Diamond, P. J., & Kemball, A. J. 1998, ASP Conf. Ser., 154, 1621
Miyoshi, M., Matsumoto, K., Kameno, S., Takaba, H., & Iwata, T. 1994, Nature, 371, 395
Monnier, J. D., et al. 2004, ApJ, 605, 436
Olofsson, H., Lindqvist, M., Nyman, L.-Å., & Winnberg, A. 1998, A&A, 329, 1059
Reid, M. J., & Menten, K., M. 2007, ApJ, 671, 2068
Reid, M. J., & Moran, J. M. 1981, ARA&A, 19, 231
Soria-Ruiz, R., Alcolea, J., Colomer, F., Bujarrabal, V., & Desmurs, J.-F. 2007, A&A, 468, L1
Soria-Ruiz, R., Alcolea, J., Colomer, F., Bujarrabal, V., Desmurs, J.-F., Marvel, K. B., & Diamond, P. J. 2004, A&A, 426, 131
Whitelock, P., Menzies, J., Feast, M., Marang, F., Carter, B., Roberts, G., Catchpole, R., & Chapman, J. 1994, MNRAS, 267, 711
Wing, R. F.,& Lockwood, G. W. 1973, ApJ, 184, 873
Wittkowski, M., Boboltz, D. A., Ohnaka, K., Driebe, T., & Scholz, M. 2007, A&A, 470, 191
Yates, J. A., & Cohen, R. J. 1994, MNRAS, 270, 958
Yi, J., Booth, R. S., Conway, J. E., & Diamond, P. J. 2005, A&A, 432, 531